scientific reports

Check for updates

OPEN

pH-responsive magnetic $CuFe_2O_4$-PMAA nanogel conjugated with amino-modified lignin for controlled breast cancer drug delivery

Nadia Fattahi[1,2], Faranak Aghaz[3], Aram Rezaei[3]✉, Ali Ramazani[1]✉, Abolfazl Heydari[4], Seyedmohammad Hosseininezhad[1] & Won-Kyo Jung[2,5,6]✉

In this study, a novel magnetic and pH-responsive nanocarrier was developed, incorporating both natural and synthetic polymers, for delivering curcumin (CUR) to breast cancer cells. For this purpose, $CuFe_2O_4$@poly(methacrylic acid) ($CuFe_2O_4$@PMAA) nanogel was developed and conjugated with amino-modified lignin (Lignin-adipic acid dihydrazide conjugate, Lig-ADH) to achieve the $CuFe_2O_4$@PMAA@Lig-ADH nanocarrier. The morphology, structure, and physical properties of the synthesized nanomaterials were examined using a range of techniques, including transmission electron microscopy (TEM), field emission scanning electron microscopy (FESEM), Fourier transform infrared (FT-IR) spectroscopy, X-ray diffraction (XRD), energy dispersive X-ray (EDX), and vibrating sample magnetometer (VSM). The synthesized nanocarrier exhibited a spherical shape, with an average diameter of approximately 15 nm, and demonstrated good magnetic responsiveness. Moreover, the in vitro drug release was found to be pH-dependent, with an increased release rate in acidic conditions. To evaluate cytotoxicity, the survival of MCF-7 cells was measured using the MTT assay for 24 h. Notably, the synthesized $CuFe_2O_4$@PMAA@Lig-ADH@CUR and CUR exhibited significant cytotoxic effects, effectively eliminating MCF-7 cells with IC_{50} values of 39.80 µg/mL and 4.27 µg/mL, respectively. Also, the significant intracellular uptake of NPs was confirmed by FITC and DAPI staining after 4 h. This research highlighted the potential of $CuFe_2O_4$@PMAA@Lig-ADH@CUR as a highly effective nano-delivery system and demonstrated a straightforward method for utilizing renewable lignin.

Keywords Nanogel, drug delivery, lignin, pH-responsive, antitumor activity

Cancer is among the most widespread and lethal diseases, marked by uncontrolled cellular growth. If untreated, it can rapidly spread to other parts of the body, significantly increasing health risks and mortality[1]. The therapeutic strategy for various cancers is primarily influenced by several key factors at the time of diagnosis, including the tumor's anatomical location, its dimensional extent, and the degree of disease progression[2].

While chemotherapy remains a primary treatment for different cancers, it faces significant challenges. It lacks specificity and commonly results in adverse side effects. Additionally, drug molecules often exhibit poor solubility in biological fluids, and cancers can develop resistance to this form of therapy over time[3,4]. Accordingly, novel strategies are urgently required to enhance tolerance and reduce the adverse effects of chemotherapy. In this regard, nanotechnology is one of the most promising candidates[5–9].

[1]The Organic Chemistry Research Laboratory (OCRL), Department of Chemistry, Faculty of Science, University of Zanjan, Zanjan 45371-38791, Iran. [2]Marine Integrated Biomedical Technology Center, The National Key Research Institutes in Universities, Pukyong National University, Busan 48513, Republic of Korea. [3]Nano Drug Delivery Research Center, Health Technology Institute, Kermanshah University of Medical Sciences, Kermanshah 67158-47141, Iran. [4]Polymer Institute of the Slovak Academy of Sciences, Dúbravská cesta 9, Bratislava 845 41, Slovakia. [5]Research Center for Marine Integrated Bionics Technology, Pukyong National University, Busan 48513, Republic of Korea. [6]Major of Biomedical Engineering, Division of Smart Healthcare and New-Senior Healthcare Innovation Center (BK21 Plus), Pukyong National University, Busan 48513, Korea. ✉email: aram.rezaei@gmail.com; aliramazani@gmail.com; wkjung@pknu.ac.kr

Nanotechnology involves designing and utilizing nanostructures that possess distinctive chemical and physical properties[10–21]. Over the past two decades, significant advancements have been made in nanotechnology-based materials, leading to the emergence of promising nanoplatforms characterized by low toxicity and high specificity in new medical technologies[22–27]. Nanomaterials have the potential to improve the effectiveness of chemotherapy drugs, potentially lowering the necessary dosage and minimizing adverse reactions[28,29]. Magnetic nanomaterials, in particular, have attracted considerable interest owing to their exceptional chemical and physical properties, making them highly promising for medical applications such as magnetic resonance imaging, drug delivery systems, and hyperthermia[30–33].

Ferrites constitute a significant category of magnetic materials known for their semiconductive properties. Nanoscale ferrites, characterized by the chemical formula MFe_2O_4 (where M can be Co, Cu, Ni, Mn, or Zn), exhibit excellent magnetic, electrical, mechanical, and chemical properties[34]. These properties make them suitable for diverse applications, including magnetic and dielectric materials, catalysis, photoluminescence, water purification, photocatalysis, corrosion protection, pigments, antimicrobial agents, sensors, and biomedical uses[35,36].

In order to achieve effective synergistic chemoradiotherapy, Salehiabar et al.[37] designed a targeted nano radiosensitizer called $CuFe_2O_4$@serum albumin-folic acid-CUR. In vitro investigations demonstrated that the synthesized nano formulation exhibited excellent biosafety, a strong ability to kill tumor cells, and effective radio sensitization. Furthermore, in vivo studies showed high efficiency in suppressing cancer[37]. In another study, Talaei et al.[38] synthesized a mesoporous nanocomposite with a core-shell nanostructure of $CuFe_2O_4$@SiO_2. The nanocomposite demonstrated efficient loading of ibuprofen and precise control over drug release. The results indicated that $CuFe_2O_4$ nanoparticles (NPs) coated with mesoporous silica exhibited low cytotoxicity and also influenced drug release properties[38].

Lignin, an amorphous polyphenol and a primary component of plant cell walls, is increasingly recognized for its potential in nanomedicine applications, particularly in cancer treatment[39,40]. This interest arises from lignin's biocompatibility, biodegradability, and chemical stability. By modifying the surface properties such as the charge or chemical functionality of lignin-based nanomaterials, these NPs can potentially be internalized by tumor cells through endocytosis or phagocytosis. This process allows for the controlled release of encapsulated drugs, reducing adverse effects and enabling targeted cancer therapy[41,42]. One notable characteristic of lignin is its abundance of functional groups, including phenolic, carboxylic, and aliphatic hydroxyl groups. These groups enable various chemical modifications and adjustments of polarity, facilitating its compatibility with appropriate polymeric matrices[43].

In recent years, researchers have increasingly focused on chemically modifying lignin for various material applications. One promising approach involves introducing reactive amino groups onto lignin. The introduction of amino groups not only improves lignin's solubility in aqueous environments but also facilitates the conjugation of various bioactive molecules, enabling the development of targeted drug delivery platforms[44]. Zhao et al.[45] developed an innovative pH-sensitive drug delivery system utilizing self-assembling polymeric NPs. This platform incorporated an aminated lignin-histidine conjugate complexed with 10-hydroxy camptothecin. The selection of lignin as a key component was driven by its inherent biocompatibility, enhancing the potential for in vivo applications[45].

PMAA nanogels have emerged as prominent carriers for bioactive agents due to their unique properties. PMAA contains abundant carboxylic acid groups within its polymer structure, allowing the nanogels to contract or swell in response to changes in pH levels in their environment. These ionizable groups enable the nanogels to expand and contract in response to pH fluctuations in their surrounding environment. Beyond their pH sensitivity, PMAA nanogels offer several advantageous features, including excellent biocompatibility, non-toxicity, adjustable size, and ease of functionalization. These attributes make PMAA nanogels an ideal candidate for targeted drug delivery systems[46,47].

To the best of our knowledge, there have been no reports on magnetic PMAA-grafted modified lignin. Herein, our team developed a novel drug-delivery nanocarrier based on $CuFe_2O_4$. @PMAA nanogel coated by aminated lignin. $CuFe_2O_4$ NPs were first synthesized. Next, $CuFe_2O_4$@PMAA was prepared via reflux-precipitation polymerization. Then, amino-modified lignin was prepared by the Mannich reaction. After that, the surface of $CuFe_2O_4$@PMAA was modified by lignin amine through chemical conjugation. Finally, pH-responsive and magnetic $CuFe_2O_4$@PMAA-Lig-ADH nanocomposite was utilized for CUR delivery (Fig. 1).

The chemical structure and morphology of the magnetic nanocarrier were characterized using FTIR, EDX, XRD, VSM, TEM, and FESEM analyses. The drug loading and pH-responsive drug release behavior of the magnetic nanocarrier were also evaluated. To evaluate cytotoxicity, the survival rate of MCF-7 cells was evaluated using the MTT assay for 24 h. Moreover, to determine the potential degradation of nanomaterials and enhance the efficiency of drug delivery, it is crucial to examine the intra-cellular uptake of nanomaterials. Under in vitro conditions, high-throughput methods such as fluorescence microscopy can precisely examine the cellular uptake of NPs. Therefore, this study investigated the uptake behavior of synthesized $CuFe_2O_4$@PMAA-Lig-ADH@CUR by MCF-7 cells.

Materials and methods

Materials

Tragacanth gum was obtained from a local health food store. Alkali lignin, *N*, *N*′-methylenebis (acrylamide) (MBA), formaldehyde solution (37 wt%), adipic acid dihydrazide (ADH), methacrylic acid (MAA), *N*, *N*′-diisopropyl carbodiimide (DIC) and 4-dimethylamino pyridine (DMAP) were purchased from Sigma-Aldrich. Biological reagents such as fetal bovine serum (FBS), phosphate-buffered saline (PBS), 3- (4,5-dimethylthiazol-2-yl)-2,5-diphenyltetrazolium bromide (MTT reagent) were obtained from Invitrogen (Carlsbad, CA, USA) and

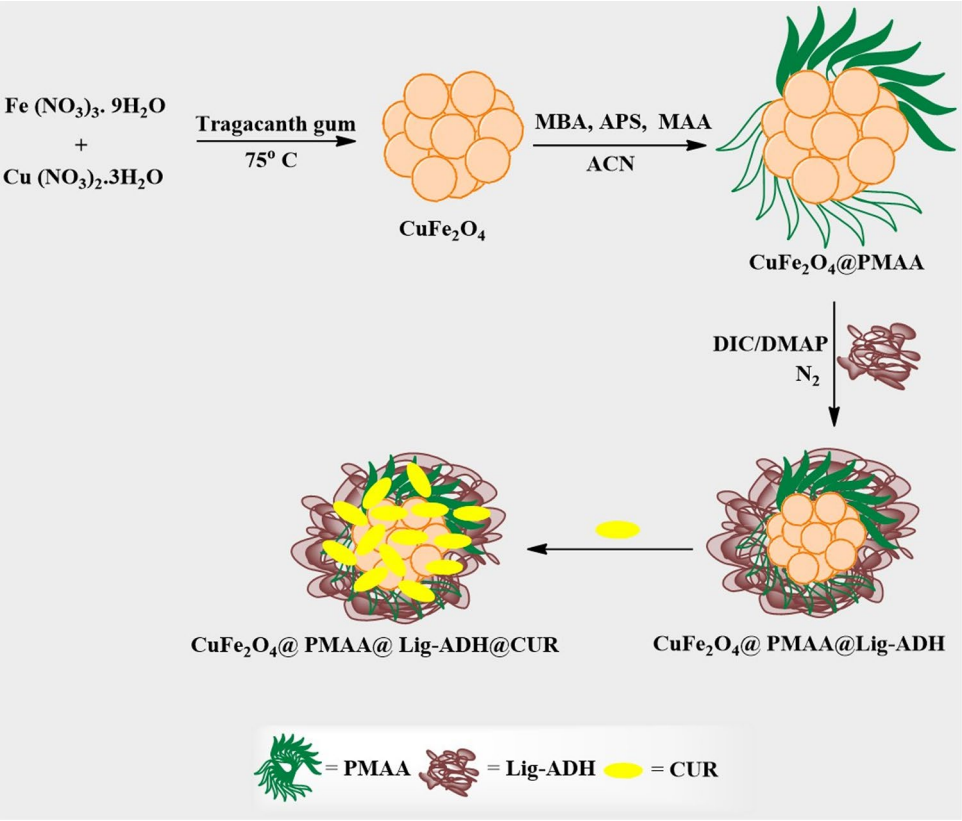

Fig. 1. Schematic synthesis of $CuFe_2O_4$@PMAA@Lig-ADH@CUR.

utilized according to their instructions. All other reagents were of analytical grade and used without further purification.

Material characterization

A Jasco 6300 FTIR spectrometer was used with KBr pellets to record the FT-IR spectra in the 400–4000 cm^{-1} range at room temperature. Structural characterization was performed using an XRD diffractometer in the range of $10° < 2\theta < 80°$, with a Cu (Kα) radiation source (wavelength of 1.5418 Å), operated at 30 mA and 40 kV. The magnetic properties were measured at room temperature using VSM (Meghnatis Kavir Kashan Co., Kashan, Iran). EDX and FESEM measurements were carried out using a SIGMA VP 500 (Zeiss) microscope. TEM imaging was performed with a Philips EM10C 200 kV microscope.

Synthesis of $CuFe_2O_4$ NPs

$CuFe_2O_4$ NPs were synthesized according to our previous method with slight modifications[48]. First, 0.2 g of tragacanth gum was dissolved in 40 ml of deionized water and stirred at 70 °C for 80 min to achieve a clear solution. Subsequently, 2 mmol of $Fe(NO_2)_2 \cdot 9\,H_2O$ and 1 mmol of $Cu(NO_2)_2 \cdot 3\,H_2O$ were added to the tragacanth gum solution. The resulting mixture was stirred for 12 h at 75 °C, yielding a brown resin. The final product was subjected to calcination in air at 600 °C for 4 h to obtain $CuFe_2O_4$ NPs.

Synthesis of $CuFe_2O_4$@PMAA

$CuFe_2O_4$@PMAA nanogels were synthesized via a typical procedure of distillation-precipitation polymerization procedure. The specified amounts used in the preparation of the nanogels were selected based on an evaluation of previous studies focused on PMAA nanogel formulations[49–51]. According to these studies and our evaluations, we identified the optimal conditions for incorporating $CuFe_2O_4$ NPs during the preparation of PMAA nanogels. Briefly, 25 mg of $CuFe_2O_4$ NPs, 53 mg of MBA, 19 mg of APS, and 0.5 mL of MAA were dissolved in acetonitrile (ACN) in a dried 50-mL single-necked flask. The mixture was subjected to ultrasound for 10 min to achieve a homogeneous suspension. The reaction mixture was then heated from ambient temperature to boiling within 30 min. The reaction was ended after approximately half of the ACN was distilled off within 1 h. The resulting $CuFe_2O_4$@PMAA nanogels were collected using ultracentrifugation at 15,000 rpm for 10 min and then dried overnight under vacuum at 50 °C.

Synthesis of Lig-ADH conjugate

0.3 g of alkali lignin was immersed in 5 mL of 0.4 M NaOH solution and stirred at room temperature to form a homogeneous solution. Then, 0.5 g of ADH and 0.7 mL of formaldehyde were added to the solution and

stirred magnetically at 60 °C for 5 h to ensure thorough mixing. Once the brown-black solution cooled to room temperature, its pH was adjusted to 5–6 using diluted HCl. Finally, Lig-ADH was collected by centrifugation, washed several times with deionized water, and dried under vacuum at 60 °C for 24 h (Fig. 2).

Synthesis of $CuFe_2O_4$@ PMAA@Lig-ADH

A carbodiimide-mediated coupling strategy was used to conjugate the amine functional groups of Lig-ADH to the carboxylic acid groups of the $CuFe_2O_4$@PMAA nanogel[52]. The procedure was as follows: 2.7 g of $CuFe_2O_4$@PMAA nanogel was dispersed in 5 mL of water and stirred vigorously overnight to ensure thorough dispersion. To activate the carboxylate groups, 0.2 mL of DIC and 15 mg of DMAP were added to the suspension, which was then stirred for 1 h at 25 °C. Following activation, Lig-ADH was slowly introduced to the activated $CuFe_2O_4$@PMAA under N_2 gas. The reaction mixture was stirred for 48 h at 40 °C to facilitate the coupling. After cooling to room temperature, the solution was dialyzed against deionized water for three days using a dialysis membrane with a molecular weight cut-off of 12,000 Da to eliminate any remaining unreacted molecules. The conjugation reaction proceeded through an amide formation.

Preparation of $CuFe_2O_4$@ PMAA@Lig-ADH@CUR

$CuFe_2O_4$@PMAA-Lig-ADH@CUR NPs were prepared using a precipitation method. In brief, 20 mg of $CuFe_2O_4$@PMAA-Lig-ADH and 5.0 mg of CUR were dissolved in 5 mL of ethanol. This ethanolic solution was then slowly added dropwise to 4.5 mL of water under vigorous magnetic stirring at 700 rpm. The reaction mixture was maintained at room temperature and stirred continuously for 12 h to ensure the complete incorporation of CUR and the formation of stable NPs. The resulting NPs were collected by centrifugation at 18,000 rpm for 30 min. To remove any unbound CUR and impurities, the NPs were washed several times with a mixture of deionized water and ethanol (75:25 v/v), followed by a final rinse with pure water. The purified $CuFe_2O_4$@PMAA-Lig-ADH@CUR NPs were then suspended in a PBS solution for further use or characterization.

Drug loading

To determine the CUR loading, 2.0 mg of $CuFe_2O_4$@PMAA-Lig-ADH@CUR NPs were dispersed in 8 mL of ethanol and incubated at 37 °C overnight to ensure complete release of physically adsorbed CUR. After incubation, the dispersion was centrifuged at 18,000 rpm for 15 min to separate the NPs from the supernatant. The absorbance of the CUR-containing supernatant was then measured using a UV-vis spectrophotometer at 428 nm. The CUR loading was calculated according to the following equations:

$$\text{Drug loading}\,(\%) = \frac{Weight\,of\,drug\,in\,NPs}{Weight\,of\,NPs} \times 100$$

The weight of the drug in NPs refers to the weight of the encapsulated drug, while the weight of NPs denotes the total weight of the corresponding drug-loaded NPs.

Drug release study

In vitro drug release was evaluated using the dialysis diffusion method. The procedure was as follows: 2 mg of the synthesized nano formulation was dispersed in 2 mL of PBS containing 1% (v/v) Tween 80. This suspension was placed in a dialysis bag with a 12 kDa molecular weight cut-off and immersed in 25 mL of PBS at 37 °C. At predetermined time intervals, 2 mL of the dialysate was withdrawn and replaced with an equal volume of fresh PBS. To assess pH-dependent drug release, the experiments were also conducted using PBS at pH 5.6. Moreover, we used free CUR as a control in the drug release studies, allowing for a direct comparison between the release profile of the encapsulated CUR and the free drug. Additionally, to ensure that the detected drug in

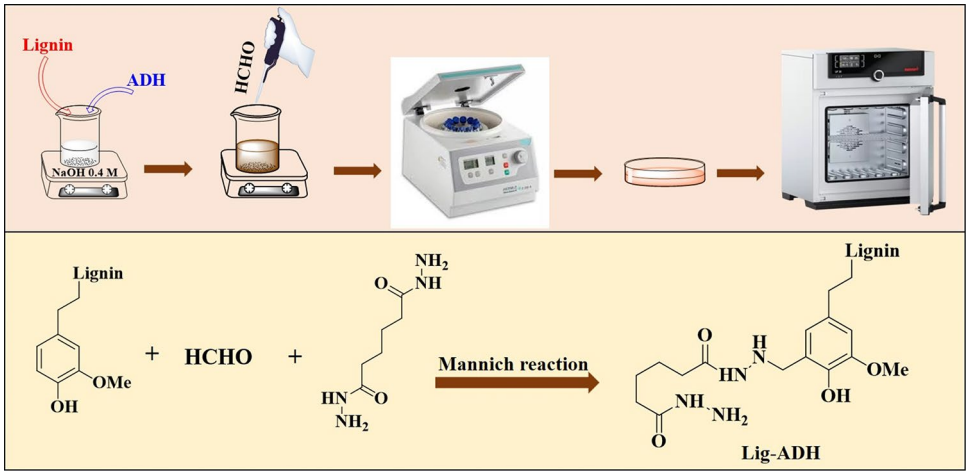

Fig. 2. Schematic representation of the synthesis of Lig-ADH conjugate.

the release medium originated solely from the encapsulated CUR, the nanogel was thoroughly washed to remove any unencapsulated drug prior to the experiments.

The concentration of CUR in the dialysate was determined using a UV-Vis spectrophotometer (Metrohm, Analytik Jena-Specord 205) at a wavelength of 428 nm, with quartz cuvettes of 1 cm optical path length (Hellma). All release studies were performed in triplicate to ensure reproducibility and statistical significance of the results.

Cytotoxicity assay

The Iranian Pasteur Institute provided the MCF-7 breast cancer cell line (NCBI Code: C135). The growth medium used for the cells was DMEM/F12 supplemented with 10% FBS, 100 µg/mL streptomycin, 100 U/mL penicillin, and 0.25 µg/mL amphotericin B. Cultures were kept at 37 °C in 5% CO_2 humidified atmosphere. The medium was changed every 48 h until cells reached 70–80% confluence. Cells were then detached using trypsin-EDTA, seeded in 96-well plates at a density of 5×10^3 cells per well, and incubated for 24 h. To evaluate the cytotoxicity, MCF-7 cells were exposed to various concentrations (10, 50, 100, 200, and 500 µg/mL) of $CuFe_2O_4$, $CuFe_2O_4$@PMAA, $CuFe_2O_4$@PMAA-Lig-ADH, $CuFe_2O_4$@PMAA-Lig-ADH@CUR, and CUR for 24 h. After treatment, cells were washed with PBS and incubated with 50 µL of MTT solution (5 mg/mL in PBS) for 4 h at 37 °C and 5% CO_2. The formazan crystals were then dissolved in 200 µL of DMSO, and absorbance was measured at 570 nm using a spectrophotometer (Lonza BioTek ELx808 Absorbance Plate Reader). Cell viability was calculated using the following formula:

$$\text{Cell viability}\,(\%) = \frac{A570\ (sample)}{A570\ (control)} \times 100$$

IC_{50} was also calculated.

Intracellular assay with FITC and nuclear evaluation by DAPI dye

First, a FITC solution (5 mg/mL) was combined with a synthesized nanoparticle suspension (1 mg/mL) and left to incubate overnight under dark conditions for fluorescent labeling. Following this, the samples were centrifuged and repeatedly washed with sterile double-distilled water (ddH_2O) until the supernatant was clear. To prepare a sufficient quantity of MCF-7 cells for intracellular analysis, 2×10^5 cells per well were incubated in a 6-well plate for 24 h.

Finally, FITC-labeled samples were introduced into MCF-7 cells at the IC_{50} concentration and incubated for 4 h to assess the cellular uptake kinetics of the synthesized sample. To evaluate the nuclear structure, DAPI (4′,6-diamidino-2-phenylindole) staining was performed. After 24 h of sample exposure, the cells were washed with PBS, fixed with 4% (v/v) paraformaldehyde for 30 min, and then rinsed twice with PBS. The cells were then stained with DAPI dye (Sigma-Aldrich, USA) and rinsed three times with PBS. Subsequently, the cells on wells ($n = 3$) were examined using a fluorescent microscope (Cytation 5 Cell Imaging Multi-Mode Reader) to visualize and analyze the cellular.

Statistical analysis

The cytocompatibility and cytotoxicity data were analyzed using GraphPad Prism version 8.0 software (GraphPad Software Inc., San Diego, CA, USA). Statistical comparisons between groups were performed using one-way analysis of variance (ANOVA). A P-value of ≤ 0.05 was considered statistically significant for all analyses.

Result and discussion

FTIR analysis

As shown in Fig. 3a, the characteristic peak of lignin at 3425 cm^{-1} corresponds to the stretching vibrations of the O–H group. The C–H bending vibrations in methyl and methylene groups caused the appearance of the peak at 1408 cm^{-1}. The stretching bands at 1600 cm^{-1} are attributed to the aromatic rings in alkali lignin, and the peak at 1123 cm^{-1} is attributed to C–O stretching. The ADH IR spectrum illustrated bands at 3314.82, 3179.58, 3047.27, 1644.34, 1532.85, and 1034.87 cm^{-1} due to the $\upsilon(NH_2)$s, $\upsilon(NH_2)$as, υ(NH), υ(C=O), amide II, and υ(N–N) vibrations, respectively (Fig. 3b)[53]. The characteristic curve of Lig-ADH exhibited several notable changes: the peaks at 2928.90 cm^{-1} and 2850.80 cm^{-1} were significantly stronger (corresponding to C-H stretch vibration in methylene), a new peak appeared at 1194.76 cm^{-1} (attributed to C-N stretching vibration), and a wider peak at 3415.98 cm^{-1} was observed due to the coexistence of O–H and N–H in Lig-ADH. Additionally, the characteristic peaks at 1663.41, 1410.28, and 1346.49 cm^{-1} were ascribed to the deformation vibrations of amide (Fig. 3c). These characteristic peaks indicate that AL-ADH has been successfully synthesized.

The FT-IR spectrum of $CuFe_2O_4$ NPs (Fig. 4a) revealed several characteristic absorption bands. The band at 579.64 cm^{-1} was attributed to the stretching vibration of tetrahedral complexes. A broad absorption band centered at 3415.58 cm^{-1} represented the stretching mode of H_2O molecules and OH groups. Additionally, the absorption band at 1617.80 cm^{-1} in the spectrum was associated with the vibration of residual H_2O in the sample[54]. CUR showed its signature peaks at 3416.73 cm^{-1} (phenolic O-H stretching vibration), 1641.72 cm^{-1} attributed predominantly to the overlapping stretching vibrations of alkenes (C=C) and carbonyl (C=O) character, C=C aromatic stretching vibration at 1402.03 cm^{-1}, 1162 cm^{-1} attributed to the bending vibration of the aromatic C–O stretching, 995.81 cm^{-1} (C–O–C stretching vibrations) (Fig. 4b)[55]. In the case of $CuFe_2O_4$@PMAA, 3227.10 cm^{-1} associated with O-H stretching, 2925.52 cm^{-1} (C-H stretching vibrations), 1701.21 cm^{-1} (C=O stretching vibration), 1420.38 cm^{-1} (C-H bending), the formation of a characteristic peak at 598.62 cm^{-1} was demonstrated (Fig. 4c).

For $CuFe_2O_4$@PMAA@Lig-ADH, 3247.53 cm^{-1} corresponds to N-H stretching vibrations, 2929.97 cm^{-1} (C-H stretching vibrations from alkyl groups), 1704.58 cm^{-1} characteristic of C=O stretching, 1521.35 cm^{-1}

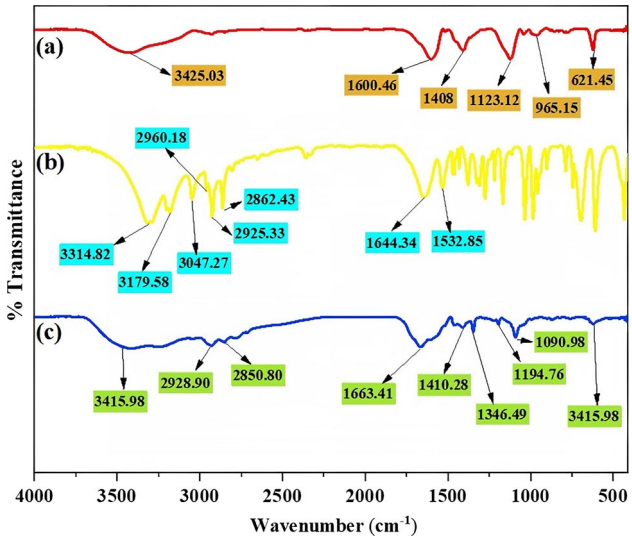

Fig. 3. FTIR spectra of (**a**) alkali lignin, (**b**) ADH, and (**c**) Lig-ADH.

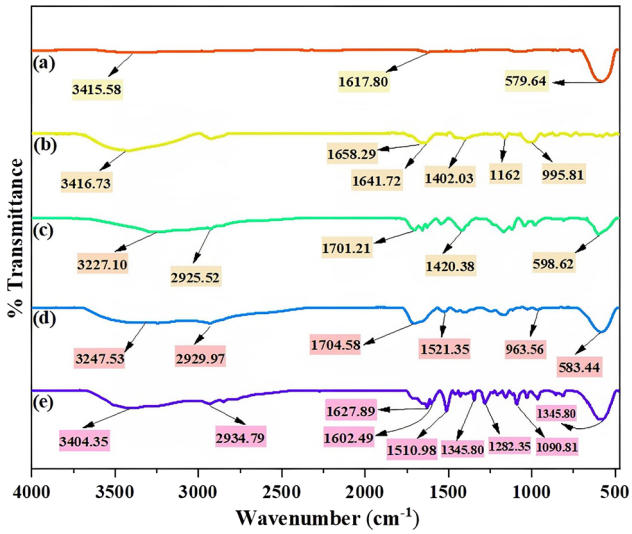

Fig. 4. FTIR spectra of (**a**) $CuFe_2O_4$, (**b**) CUR, (**c**) $CuFe_2O_4$@PMAA, (**d**) $CuFe_2O_4$@ PMAA@Lig-ADH, and (**e**) $CuFe_2O_4$@ PMAA@Lig-ADH@CUR NPs.

associated C = C stretching in aromatic rings, 1447 cm^{-1} (C-H bending in methyl groups), 1410.07 cm^{-1} indicate O-H bending in carboxylic acids, 1245.33 cm^{-1}, 1164.95 cm^{-1} and 1026.52 cm^{-1} Suggests C-O stretching, 963.56 cm^{-1} associated with = C-H bending, and the formation of a characteristic peak at 583.44 cm^{-1} was demonstrated (Fig. 4d).

For $CuFe_2O_4$@PMAA@Lig-ADH@CUR NPs, 3404.35 cm^{-1} associated with O-H stretching vibrations, 2934.79 cm^{-1} (C-H stretching vibrations from methyl), 1627.89 cm^{-1} indicative C = O stretching in amides, 1602.49 cm^{-1} associated with C = C stretching vibrations from an aromatic ring, 1510.98 cm^{-1} (N-O asymmetric stretch), 1429.20 cm^{-1} (C-H bending vibrations), 1345.80 cm^{-1} (Symmetric NO_2 stretching), 1282.35 cm^{-1} (C-O stretching), 1154.30 cm^{-1} (C-N stretching vibrations in amines), 1090.81 cm^{-1} (C-O-C stretching vibrations), 963.84 cm^{-1} indicative of = C-H bending, 814.59 cm^{-1} (Out-of-plane bending vibrations of substituted aromatic compounds), and 576.71 cm^{-1} (Metal-oxygen stretching vibrations) (Fig. 4e).

FESEM, TEM, and zeta potential analyses

The FESEM image presented in Fig. 5a clearly shows the $CuFe_2O_4$@PMAA@Lig-ADH composite. From the FESEM imaging, we can deduce that the $CuFe_2O_4$@PMAA@Lig-ADH was successfully synthesized in situ alongside Lig-ADH, as evidenced by the spherical morphology of the sample. In contrast, the TEM image reveals that the synthesized nanocarrier is smaller than the FESEM image. The $CuFe_2O_4$@PMAA@Lig-ADH particles had an average diameter of approximately 15 nm (Fig. 5b). According to the literature, $CuFe_2O_4$ has a

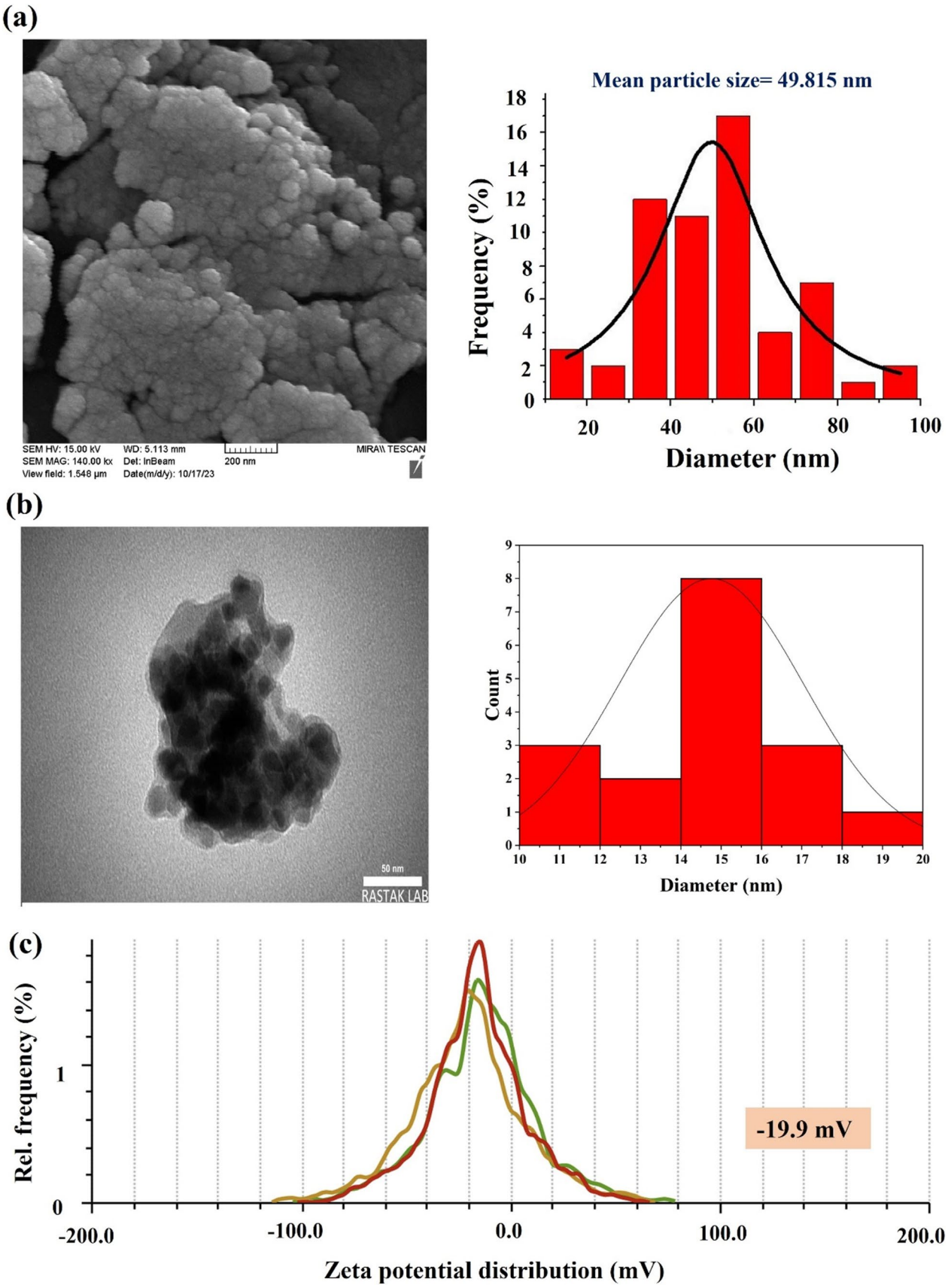

Fig. 5. (**a**) FESEM image and corresponding size distribution histogram of $CuFe_2O_4$@PMAA@Lig-ADH, (**b**) TEM image and corresponding size distribution histogram of $CuFe_2O_4$@PMAA@Lig-ADH, and (**c**) Zeta potential analysis of $CuFe_2O_4$@PMAA@Lig-ADH@CUR.

spherical shape[54] and it appears in the mentioned composite FESEM and TEM. It has also been reported that when different methods are used for the synthesis of $CuFe_2O_4$ magnetic NPs, it is effective in their size[56].

The zeta potential is a critical factor in determining the stability of colloidal system. When particles in suspension possess a uniform charge, either all negative or all positive, electrostatic repulsion between them prevents aggregation, thereby enhancing the system's stability. This repulsion is directly tied to the zeta potential, which influences not only the suspension's stability but also the behavior of NPs in biological systems, such as their circulation in the bloodstream and their interaction or adhesion to cell layers. In this study, the zeta potential of $CuFe_2O_4$@PMAA@Lig-ADH@CUR was determined to be -19.9 mV (Fig. 5c).

This negative charge, combined with the nanoparticle's small size of 15 nm, as measured by TEM analysis, makes $CuFe_2O_4$@PMAA@Lig-ADH@CUR a promising candidate for various biomedical applications, including in vitro, in vivo, and preclinical studies.

EDX and mapp analysis

The EDX spectrum depicted in Fig. 6a for the $CuFe_2O_4$@PMAA@Lig-ADH composite demonstrated that the Cu and Fe elements were predominantly incorporated within the nanocomposites as a $CuFe_2O_4$. The presence of PMAA and Lig-ADH were validated by the peaks of C and O. Additionally, the peaks corresponding to O and C may also be indicative of the presence of $CuFe_2O_4$. Based on the literature, the concentrations of copper and iron

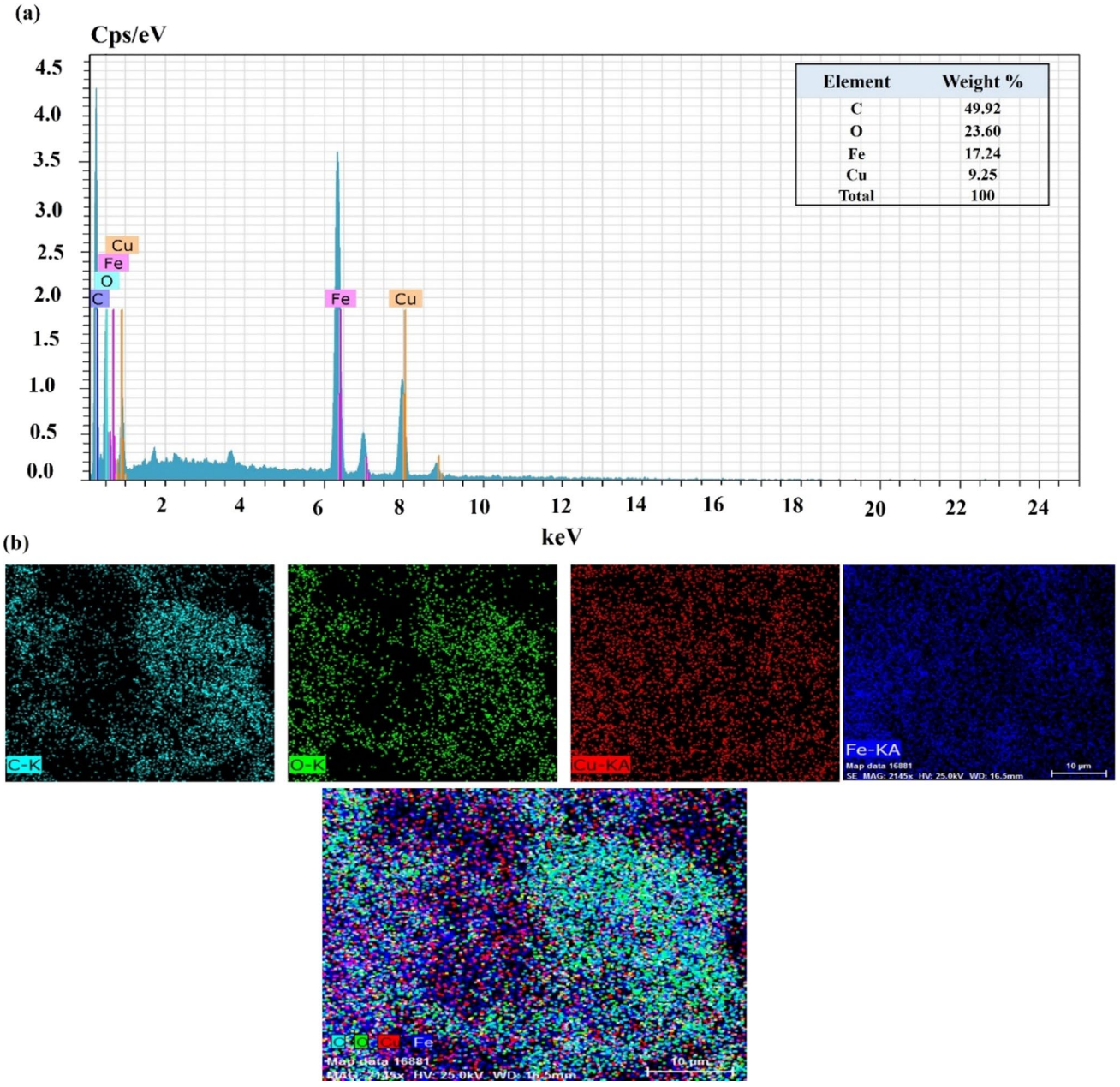

Fig. 6. (**a**) EDX analysis and (**b**) element mapping of $CuFe_2O_4$@PMAA@Lig-ADH.

in $CuFe_2O_4$ NPs were determined to be 4.25 mmol/g and 7.67 mmol/g, respectively, using ICP-AES[54]. Also, in the literature, according to EDX studies, it has been shown that the atomic percentage is close to stoichiometry. For example, for $CuFe_2O_4$ NPs, a ratio of 1:2:4 has been reported for Cu: Fe: O: respectively[56]. Map analysis further corroborated the elemental distribution, revealing that the Cu and Fe elements were homogeneously dispersed throughout the $CuFe_2O_4$@PMAA@Lig-ADH composite (Fig. 6b).

VSM analysis

Figure 7 presents the magnetization curves for both $CuFe_2O_4$ and $CuFe_2O_4$@PMAA@Lig-ADH. It is evident that each sample exhibits ferrimagnetic characteristics, complete with a hysteresis loop. The saturation magnetization values were approximately 15 emu/g for $CuFe_2O_4$ and 5.5 emu/g for $CuFe_2O_4$@PMAA@Lig-ADH. Of course, this amount is also reported as 29.34 emu/g[48] and 45 emu/g[54] for $CuFe_2O_4$-NPs in the literature. In a study, the saturation magnetization value of Fe_3O_4@PMAA composite was reported 40.4 emu/g[57].

The saturation magnetization in spinel ferrites can be attributed to the distribution of cations. Specifically, $CuFe_2O_4$ is a reverse spinel containing two types of magnetic cations: Cu^{2}+ and Fe^{3}+. Within the structure, half of the Fe^{3}+ ions are situated in tetrahedral positions, while the remainder, along with all Cu^{2}+ ions, are located in octahedral sites.

XRD pattern

Figure 8 displays the XRD pattern for the $CuFe_2O_4$ MNPs. The XRD analysis reveals distinct diffraction peaks at 2θ values of 30.25°, 35.88°, 37.50°, 43.06°, 54.07°, 57.51°, and 62.69°, which correspond to the crystallographic planes (220), (311), (222), (400), (422), (511), and (440), respectively. These peaks confirm the formation of a pure cubic structured ferrite, as indicated by the JSPDS Card no. 75-1517, with lattice parameters a = b = c = 8.341 Å. The observed diffraction pattern aligns well with the literature[48,58], which also reported similar peak positions for $CuFe_2O_4$ NPs, confirming the consistency of our findings with previous studies. Importantly, our XRD analysis shows no signs of extraneous impurity peaks, further supporting the purity of the synthesized NPs. X-ray diffraction studies on standard PMAA adsorbent reveal, as documented in the literature, that the diffractogram is devoid of distinct peaks across the entire 2θ spectrum. This indicates the polymer's lack of crystallinity, classifying it as an amorphous solid. Existing studies indicate that the XRD pattern for electrospun lignin is characterized by a distinct diffraction peak at a 2θ = 17°[59]. The presence of this peak in the X-ray diffraction of $CuFe_2O_4$@PMAA@Lig-ADH demonstrates that lignin has been successfully incorporated into the composite structure.

Drug loading and in vitro release study

The CUR loading mechanism in $CuFe_2O_4$@PMAA@Lig-ADH involves a combination of physical adsorption and chemical interactions. Lig-ADH functionalized $CuFe_2O_4$@PMAA nanogel contributes to the formation of π-π stacking interactions and hydrogen bonds with CUR, which promote effective loading. Additionally, the PMAA component provides a hydrophilic environment that enhances the solubility of CUR and facilitates its diffusion into the polymer matrix. The loading capacity of $CuFe_2O_4$@PMAA@Lig-ADH@CUR was calculated to be 11.55 ± 0.41.

The in vitro release profile of CUR from the synthesized $CuFe_2O_4$@PMAA-Lig-ADH nanocarrier was investigated over a 120-hour period. The study was conducted in PBS at two distinct pH levels: 7.4 and 5.6, with the addition of 1% (v/v) Tween 80 to enhance CUR solubility. The neutral pH of 7.4 was chosen to simulate blood and plasma conditions, representing the environment encountered during intravenous administration. Conversely, the acidic pH of 5.6 was selected to mimic the tumor microenvironment, which is characteristically

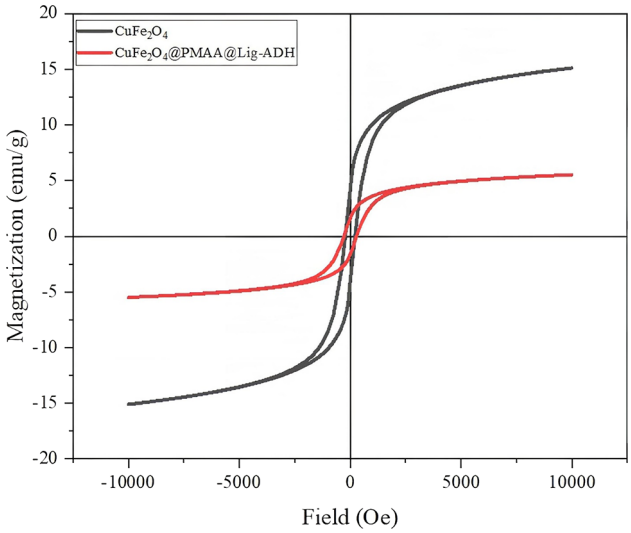

Fig. 7. Magnetization curve of $CuFe_2O_4$ and $CuFe_2O_4$@PMAA@Lig-ADH.

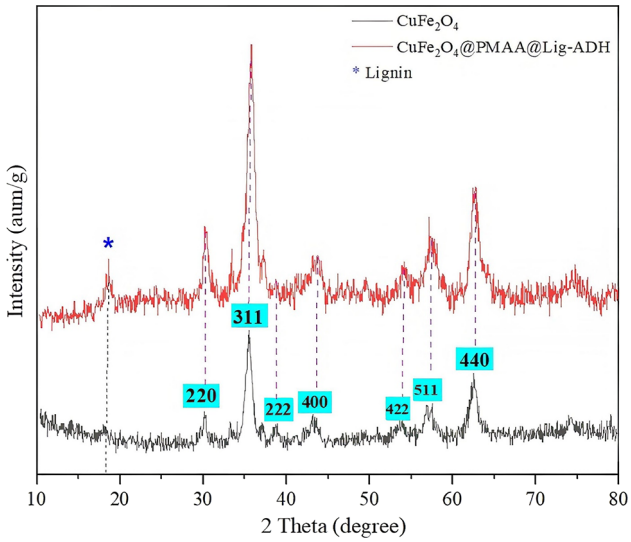

Fig. 8. XRD Spectrum of $CuFe_2O_4$ and $CuFe_2O_4$@PMAA@Lig-ADH.

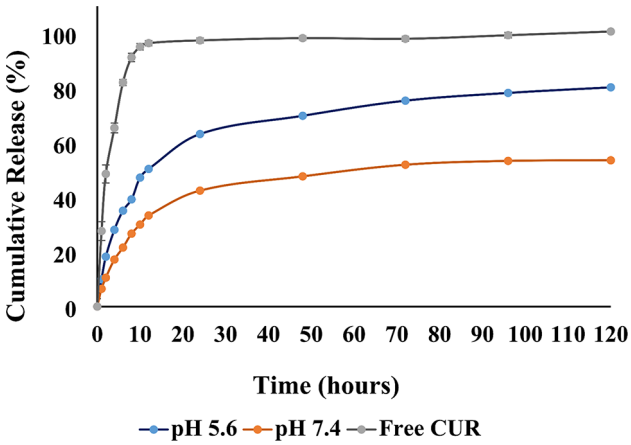

Fig. 9. In vitro release of CUR from $CuFe_2O_4$@PMAA-Lig-ADH@CUR at pH 5.6 and 7.4, and free CUR (Data represent mean ± SD; $n = 3$).

more acidic than normal tissues. The development of a pH-responsive drug delivery system is a very promising strategy for cancer treatment, as the pH of the tumor microenvironment is lower than that of normal tissue. Additionally, this method can enhance drug accumulation in tumor tissues as opposed to normal tissues and lessen the adverse effects of chemotherapy.

Figure 9 illustrates the drug release profile of CUR from the $CuFe_2O_4$@PMAA-Lig-ADH nanocarrier, demonstrating a pH-dependent release behavior in a sustained and controlled manner. The release of CUR was faster under acidic conditions compared to normal physiological conditions. Approximately 79% of CUR was released from the nanocarrier at pH 5.6 after 120 h, whereas at physiological pH (7.4), around 50% of the loaded CUR was released. The observed controlled release behavior can be attributed to the interaction between CUR and the nanocarrier matrix, which likely slows the diffusion of CUR from the nanoparticle core. In comparison, the release profile of free CUR, which served as a control, showed rapid release kinetics under identical conditions. This rapid release highlights the diffusion of unencapsulated CUR and serves as a baseline for the release kinetics of CUR in the absence of the nanocarrier. By comparing these profiles, it was confirmed that the CUR detected in the release medium from the nanoformulation study originated solely from the encapsulated drug. The control study thus rules out any potential contribution from free CUR, reinforcing the conclusion that the nanocarrier effectively encapsulated and modulated the release of CUR.

In-vitro cytotoxicity assay

In vitro cytotoxicity tests on MCF-7 cells at different concentrations (10, 50, 100, 200, and 500 µgmL−[1]), were conducted to assess the synthesized nanoparticle cytotoxicity. In the cytotoxicity method during 24 h, $CuFe_2O_4$@PMAA-Lig-ADH@CUR and CUIR demonstrated higher toxicity activity than $CuFe_2O4$, $CuFe_2O_4$@PMAA, and

$CuFe_2O_4$@PMAA-Lig-ADH in all concentrations (Fig. 10). Based on our results, it is clear that the IC_{50} dose for $CuFe_2O_4$, $CuFe_2O_4$@PMAA, and $CuFe_2O_4$@PMAA-Lig-ADH was 194.26, 498.96, and 482.72 μgmL−1, while the IC_{50} was (39.80 and 4.27 μgmL-1), when MCF-7 cells were treated with $CuFe_2O_4$@PMAA-Lig-ADH@CUR and CUR. Also, significant toxicity was observed for both the $CuFe_2O_4$@PMAA-Lig-ADH@CUR and CUR at all concentrations after incubation for 24 h, which decrease in cell viability was more obvious in Cur (Fig. 10). Despite administering a low dose of CUR (10 μgmL−1), the cell viability percentage of MCF-7 cells significantly decreased. Interestingly, a similar decrease was observed with $CuFe_2O_4$@PMAA-Lig-ADH@CUR at comparable concentrations. The anti-cancer property of the CUR is likely to account for its awful toxicity effect. Notably, our synthesized NPs exhibit controlled release of pure CUR, confirming their cytocompatibility for in vivo biomedical applications.

Intracellular uptake kinetics evaluated by fluorescent microscopy

To highlight the key steps and interactions that lead to increased cell cytotoxicity of a nanoparticle, we can break down the process into several critical components: The first and most important test is "nanoparticle uptake and accumulation" which is the main aim of our study and analyzed it by FITC-conjugation and followed it with a fluorescent microscope (Fig. 11). For the evaluation of cell cytotoxicity, the nanoparticle must be efficiently taken up by the target cells, firstly. This can occur through passive diffusion, active transport, or endocytosis. Once inside the cell, the nanoparticle accumulates to a concentration sufficient to exert its cytotoxic effects. By understanding this key step, researchers can better design nano-drugs to maximize their cytotoxic effects while minimizing side effects. So, we evaluated intracellular uptake and nuclear effects of both the $CuFe_2O_4$@PMAA-Lig-ADH, and $CuFe_2O_4$@PMAA-Lig-ADH@CUR samples using its IC_{50} dosage (39.80 and 4.27 μgmL-1). The Cytation 5 Cell Imaging Multi-Mode Reader was employed for fluorescence microscope imaging to assess the morphology of MCF-7 cells. These cells were exposed to FITC-labeled $CuFe_2O_4$@PMAA-Lig-ADH, and $CuFe_2O_4$@PMAA-Lig-ADH@CUR for 4 h. The resulting image revealed that most of the FITC-labeled synthesized NPs were taken up by MCF-7 cells via endocytosis. The green fluorescence observed throughout the cytoplasm indicated that the $CuFe_2O_4$@PMAA-Lig-ADH, and $CuFe_2O_4$@PMAA-Lig-ADH@CUR were internally localized within the cells. These initial findings have significant implications for biomedical applications, particularly in the realm of intracellular drug delivery. The study highlights the anticancer effect and rapid internalization potential of $CuFe_2O_4$@PMAA-Lig-ADH, and $CuFe_2O_4$@PMAA-Lig-ADH@CUR nanomaterials. To delve deeper, the researchers employed DAPI staining to investigate the apoptosis-inducing properties of these nanomaterials, alongside their anticancer effect. Surprisingly, the synthesized $CuFe_2O_4$@PMAA-Lig-ADH NPs were found to be non-toxic to DNA compared to $CuFe_2O_4$@PMAA-Lig-ADH@CUR. However, they did exhibit a decrease in cellular viability and fragmentation of chromatin. The merged fluorescent DAPI and FITC images further confirmed both their anticancer effect (Fig. 11).

The specific mechanisms by which these nanogels increase ROS involve interactions at the cellular level, possibly through the generation of free radicals or interference with cellular antioxidant systems[60]. Previous published papers showed that the $CuFe_2O_4$@PMAA nanogel has been studied for its effects on reactive oxygen species (ROS) in cell cultures[60,61]. These nanogels, when conjugated with amino-modified lignin, can increase ROS levels in cells. This increase in ROS can lead to oxidative stress, which can induce apoptosis (programmed

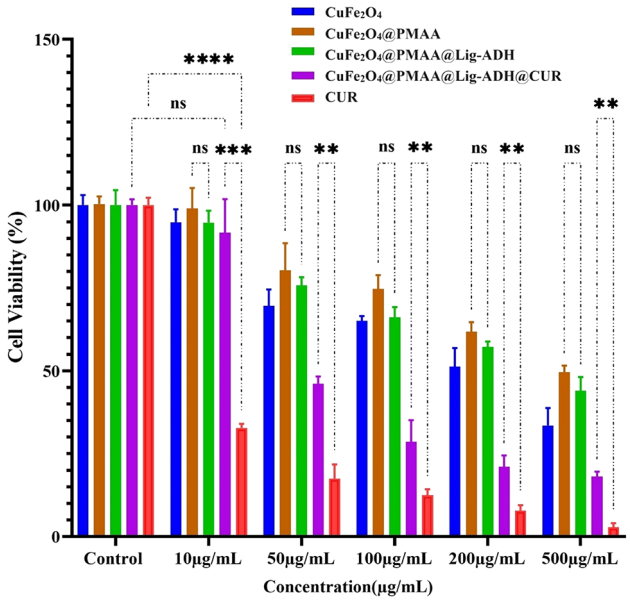

Fig. 10. Cell viability percentage graph of MCF-7 cell after treatment with optimal concentrations of $CuFe_2O_4$, $CuFe_2O_4$@PMAA, $CuFe_2O_4$@PMAA-Lig-ADH, $CuFe_2O_4$@PMAA-Lig-ADH@CUR, and CUR; the error barres in all columns are reported as mean ± SEM (*** = $P<0.001$, ** = $P<0.01$, * = $P<0.05$).

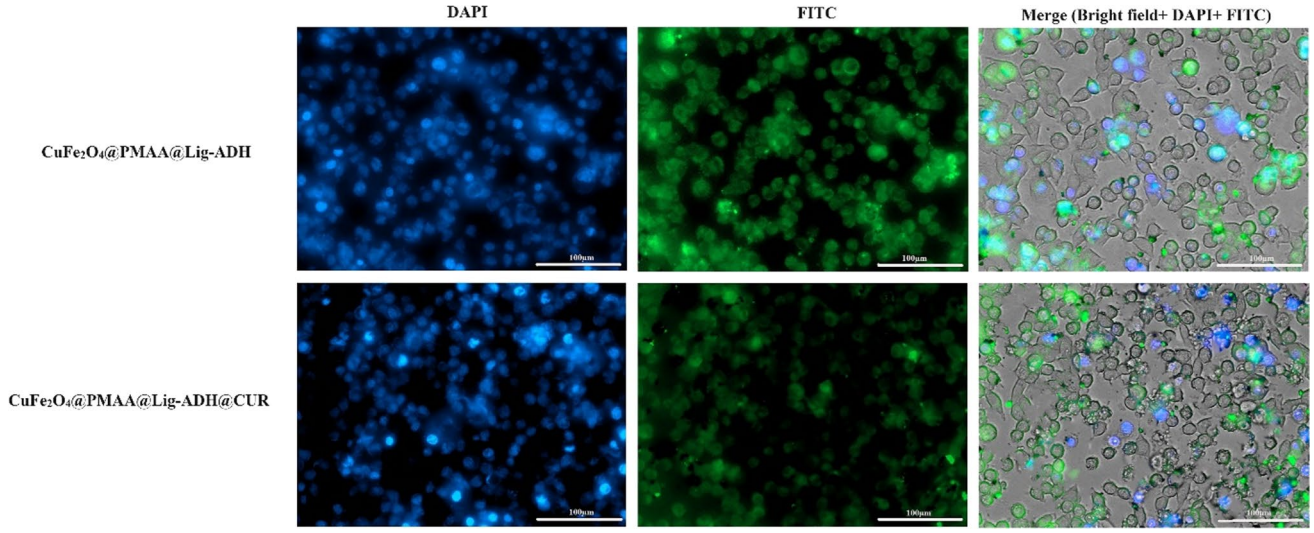

Fig. 11. Fluorescent microscopy images for intracellular uptake and nuclear effects of $CuFe_2O_4$@PMAA-Lig-ADH, and $CuFe_2O_4$@PMAA-Lig-ADH@CUR samples.

cell death), leading to potential cytotoxic effects in cancer cells. So according to our result, this nanogel is potentially useful in cancer therapies.

Conclusion

In summary, we synthesized magnetic and pH-sensitive nanocarrier based on $CuFe_2O_4$@PMAA coated with a lignin-ADH conjugate ($CuFe_2O_4$@ PMAA@Lig-ADH) for efficient CUR delivery to breast cancer cells. The synthesized nanocarrier exhibited a spherical shape, with an average diameter of approximately 15 nm, and demonstrated good magnetic responsiveness. The in vitro drug release of synthesized NPs was evaluated under both neutral (pH 7.4) and acidic (pH 5.6) conditions. The in vitro drug release was pH-dependent and increased in an acidic medium, confirming the significant potential of nanocarrier for in vivo biomedical applications. The cytotoxicity of synthesized compounds, including $CuFe_2O_4$, $CuFe_2O_4$@PMAA, $CuFe_2O_4$@PMAA-Lig-ADH, $CuFe_2O_4$@PMAA-Lig-ADH@CUR and CUR was evaluated using the MTT method on MCF-7 cells at 10, 50, 100, 200, and 500 µg/mL. Notably, $CuFe_2O_4$@PMAA@Lig-ADH@CUR and CUR exhibited higher toxicity compared to $CuFe_2O_4$, $CuFe_2O_4$@PMAA, and $CuFe_2O_4$@PMAA@Lig-ADH across all concentrations. Specifically, the IC_{50} values for $CuFe_2O_4$, $CuFe_2O_4$@PMAA, and $CuFe_2O_4$@PMAA@Lig-ADH were 194.26, 498.96, and 482.72 µg/mL, respectively. In contrast, the IC_{50} values for $CuFe_2O_4$@PMAA@Lig-ADH@CUR and Cur were significantly lower at 39.80 and 4.27 µg/mL, respectively, when treating MCF-7 cells. This work demonstrated that $CuFe_2O_4$@PMAA @Lig-ADH@CUR NPs provides beneficial potential in targeting the delivery of antitumor drugs and applications into the cancer therapy by FITC and DAPI stain.

Data availability

All the associated with this work are presented here and further will be made available on reasonable request. Correspondence and requests for materials should be addressed to A.R.

Received: 8 July 2024; Accepted: 22 October 2024
Published online: 29 October 2024

References

1. Jones, P. A. & Baylin, S. B. The epigenomics of cancer. *Cell* **128**, 683–692 (2007).
2. Bodaghi, A., Fattahi, N. & Ramazani, A. Biomarkers: Promising and valuable tools towards diagnosis, prognosis and treatment of Covid-19 and other diseases. *Heliyon* **9** (2023).
3. Senapati, S., Mahanta, A. K., Kumar, S. & Maiti, P. Controlled drug delivery vehicles for cancer treatment and their performance. *Signal Transduct. Target. Ther.* **3**, 7 (2018).
4. Fattahi, N. et al. Enhancement of the brain delivery of methotrexate with administration of mid-chain ester prodrugs: In vitro and in vivo studies. *Int. J. Pharm.* **600**, 120479 (2021).
5. Qu, X. et al. Cancer nanomedicine in preoperative therapeutics: Nanotechnology-enabled neoadjuvant chemotherapy, radiotherapy, immunotherapy, and phototherapy. *Bioact. Mater.* **24**, 136–152 (2023).
6. Fattahi, N. & Ramazani, A. Nanodiamonds as next generation carriers in exploring therapeutic benefits. In *Carbon Nanostructures in Biomedical Applications* 27–66 (Springer, 2023).
7. Rezaei, A. & Hashemi, E. A pseudohomogeneous nanocarrier based on carbon quantum dots decorated with arginine as an efficient gene delivery vehicle. *Sci. Rep.* **11**, 13790 (2021).
8. Adibi-Motlagh, B., Lotfi, A. S., Rezaei, A. & Hashemi, E. Cell attachment evaluation of the immobilized bioactive peptide on a nanographene oxide composite. *Mater. Sci. Eng. C* **82**, 323–329 (2018).
9. Rezaei, A., Akhavan, O., Hashemi, E. & Shamsara, M. Toward chemical perfection of graphene-based gene carrier via Ugi multicomponent assembly process. *Biomacromolecules* **17**, 2963–2971 (2016).

10. Fattahi, N. et al. Emerging insights on drug delivery by fatty acid mediated synthesis of lipophilic prodrugs as novel nanomedicines. *J. Control Release* **326**, 556–598 (2020).
11. Malekzadeh, A. M., Ramazani, A., Rezaei, S. J. T. & Niknejad, H. Design and construction of multifunctional hyperbranched polymers coated magnetite nanoparticles for both targeting magnetic resonance imaging and cancer therapy. *J. Colloid Interface Sci.* **490**, 64–73 (2017).
12. Rad-Faraji, M. et al. A comparative study of structural and catalytic activity alterations in firefly luciferase induced by carbon quantum dots containing amine and carboxyl functional groups. *Int. J. Biol. Macromol.***260**, 129503 (2024).
13. Zarei, A. et al. Selective and sensitive CQD-based sensing platform for Cu2+ detection in Wilson's disease. *Sci. Rep.* **14**, 13183 (2024).
14. Rashidi, M. et al. Microfibers nanocomposite based on polyacrylonitrile fibers/bismuth oxide nanoparticles as X-ray shielding material. *J. Appl. Polym. Sci.* **138**, 50755 (2021).
15. Hadian-Dehkordi, L. et al. DNA-metal composites as bioinspired catalysts in chemical reactions. *Coord. Chem. Rev.* **505**, 215635 (2024).
16. Targhan, H. et al. Adsorptive and photocatalytic degradation of imidacloprid pesticide from wastewater via the fabrication of ZIF-CdS/Tpy quantum dots. *Chem. Eng. J.* **482**, 148983 (2024).
17. Targhan, H. et al. Palladium-based pseudohomogeneous catalyst for highly selective aerobic oxidation of benzylic alcohols to aldehydes. *Sci. Rep.* **14**, 536 (2024).
18. Rezaei, A., Zheng, H., Majidian, S., Samadi, S. & Ramazani, A. Chiral pseudohomogeneous catalyst based on amphiphilic carbon quantum dots for the enantioselective Kharasch–Sosnovsky reaction. *ACS Appl. Mater. Interfaces* **15**, 54373–54385 (2023).
19. Rezaei, A., Mohammadi, Y., Ramazani, A. & Zheng, H. Ultrasound-assisted pseudohomogeneous tungstate catalyst for selective oxidation of alcohols to aldehydes. *Sci. Rep.* **12**, 3367 (2022).
20. Rezaei, A., Ramazani, A., Gouranlou, F. & Woo Joo, S. Silica nanoparticles/nanosilica sulfuric acid as a reusable catalyst for fast, highly efficient and green synthesis of 2-(heteroaryl) acetamide derivatives. *Lett. Org. Chem.* **14**, 86–92 (2017).
21. Ramazani, A. et al. Silica gel promotes cascade synthesis of 2-(heteroaryl) acetamide derivatives from isocyanides, dialkylamines, and heteroarylcarbaldehydes. *Synth. Commun.* **41**, 1444–1454 (2011).
22. Chenthamara, D. et al. Therapeutic efficacy of nanoparticles and routes of administration. *Biomater. Res.* **23**, 20 (2019).
23. Jain, V. et al. A review of nanotechnology-based approaches for breast cancer and triple-negative breast cancer. *J. Control Release* **326**, 628–647 (2020).
24. Fattahi, N. et al. PEI-based functional materials: fabrication techniques, properties, and biomedical applications. *Adv. Colloid Interface Sci.* 103119 (2024).
25. Saedi, Z. et al. A label-free sensor array based on carbon quantum dots for detection of α-synuclein oligomers in Saliva. *Anal. Chem.* **96**, 12246–12253 (2024).
26. Adibi-Motlagh, B. et al. Immobilization of modular peptides on graphene cocktail for differentiation of human mesenchymal stem cells to hepatic-like cells. *Front. Chem.* **10** (2022).
27. Rezaei, A., Hamad, M. A., Adibi, H., Zheng, H. & Qadir, K. H. Chiral discrimination of l-DOPA vial/d-tryptophan decorated carbon quantum dots. *Mater. Adv.* **5**, 1614–1625 (2024).
28. Ali, I., Salim, K., A Rather, M., Wani, A. & Haque, W. Advances in nano drugs for cancer chemotherapy. *Curr. Cancer Drug Targets* **11**, 135–146 (2011).
29. Krukiewicz, K. & Zak, J. K. Biomaterial-based regional chemotherapy: Local anticancer drug delivery to enhance chemotherapy and minimize its side-effects. *Mater. Sci. Eng. C* **62**, 927–942 (2016).
30. Anjum, T. et al. Magnetic nanomaterials as drug delivery vehicles and therapeutic constructs to treat cancer. *J. Drug Deliv. Sci. Technol.* **80**, 104103 (2023).
31. Mohsin, A. et al. Recent advances of magnetic nanomaterials for bioimaging, drug delivery, and cell therapy. *ACS Appl. Nano Mater.* **5**, 10118–10136 (2022).
32. Ahankar, H. et al. Tetramethylguanidine-functionalized silica-coated iron oxide magnetic nanoparticles catalyzed one-pot three-component synthesis of furanone derivatives. *J. Chem. Sci.* **130**, 1–13 (2018).
33. Hosseini Sadr, S., Davaran, S., Alizadeh, E., Salehi, R. & Ramazani, A. Enhanced anticancer potency by thermo/pH-responsive PCL-based magnetic nanoparticles. *J. Biomater. Sci. Polym. Ed.* **29**, 277–308 (2018).
34. Jadhav, V. V., Shirsat, S. D., Tumberphale, U. B. & Mane, R. S. Properties of ferrites. In *Spinel Ferrite Nanostructures for Energy Storage Devices* 35–50 (Elsevier, 2020).
35. Amiri, M., Salavati-Niasari, M. & Akbari, A. Magnetic nanocarriers: Evolution of spinel ferrites for medical applications. *Adv. Colloid Interface Sci.* **265**, 29–44 (2019).
36. Kaur, M. & Kaur, N. Ferrites: Synthesis and applications for environmental remediation. In *Ferrites and Ferrates: Chemistry and Applications in Sustainable Energy and Environmental Remediation* 113–136 (ACS, 2016).
37. Salehiabar, M. et al. Targeted $CuFe_2O_4$ hybrid nanoradiosensitizers for synchronous chemoradiotherapy. *J. Control Release* **353**, 850–863 (2023).
38. Talaei, M., Hassanzadeh-Tabrizi, S. & Saffar-Teluri, A. Synthesis of mesoporous $CuFe_2O_4$@ SiO_2 core-shell nanocomposite for simultaneous drug release and hyperthermia applications. *Ceram. Int.* **47**, 30287–30297 (2021).
39. Sathasivam, T. et al. Nano-strategies for lignin biomaterials toward cancer therapy. *Adv. Healthc. Mater.* **12**, 2300024 (2023).
40. Fattahi, N., Fattahi, T., Kashif, M., Ramazani, A. & Jung, W-K. Lignin: A valuable and promising bio-based absorbent for dye removal applications. *Int. J. Biol. Macromol.* 133763 (2024).
41. Wijaya, C. J., Ismadji, S. & Gunawan, S. A review of lignocellulosic-derived nanoparticles for drug delivery applications: Lignin nanoparticles, xylan nanoparticles, and cellulose nanocrystals. *Molecules* **26**, 676 (2021).
42. Chio, C., Sain, M. & Qin, W. Lignin utilization: A review of lignin depolymerization from various aspects. *Renew. Sustain. Energy Rev.* **107**, 232–249 (2019).
43. Agustiany, E. A. et al. Recent developments in lignin modification and its application in lignin-based green composites: A review. *Polym. Compos.* **43**, 4848–4865 (2022).
44. Li, Y. et al. Antimicrobial peptide-inspired design of amino-modified lignin with Improved antimicrobial activities. *Biomacromolecules* **24**, 5381–5393 (2023).
45. Zhao, J. et al. Self-assembled pH-responsive polymeric nanoparticles based on lignin-histidine conjugate with small particle size for efficient delivery of anti-tumor drugs. *Biochem. Eng. J.* **156**, 107526 (2020).
46. Markovic, M. D. et al. Green pH-and magnetic-responsive hybrid hydrogels based on poly (methacrylic acid) and Eucalyptus wood nanocellulose for controlled release of ibuprofen. *Cellulose* **28**, 11109–11132 (2021).
47. Zhang, Y., Gu, W., Zhao, J. & Qin, Z. A facile, efficient and green route to pH-responsive crosslinked poly (methacrylic acid) nanoparticles. *Colloids Surf. A: Physicochem. Eng. Asp.* **531**, 1–8 (2017).
48. Ramazani, A., Taghavi Fardood, S., Hosseinzadeh, Z., Sadri, F. & Joo, S. W. Green synthesis of magnetic copper ferrite nanoparticles using tragacanth gum as a biotemplate and their catalytic activity for the oxidation of alcohols. *Iran. J. Catal.* **7**, 181–185 (2017).
49. Mozafari, F. et al. Enhancing the neuroprotection potential of edaravone in transient global ischemia treatment with glutathione-(GSH-) conjugated poly (methacrylic acid) nanogel as a promising carrier for targeted brain drug delivery. *Oxid. Med. Cell. Longev.* **2023**, 7643280 (2023).
50. Rashidzadeh, H. et al. Targeted co-delivery of methotrexate and chloroquine via a pH/enzyme-responsive biocompatible polymeric nanohydrogel for colorectal cancer treatment. *J. Biomater. Sci. Polym. Ed.* **34**, 1824–1842 (2023).

51. Rashidzadeh, H., Rezaei, S. J. T., Danafar, H. & Ramazani, A. Multifunctional pH-responsive nanogel for malaria and cancer treatment: Hitting two targets with one arrow. *J. Drug Deliv. Sci. Technol.* **76**, 103740 (2022).
52. Fattahi, N., Ayubi, M. & Ramazani, A. Amidation and esterification of carboxylic acids with amines and phenols by N, N′-diisopropylcarbodiimide: A new approach for amide and ester bond formation in water. *Tetrahedron* **74**, 4351–4356 (2018).
53. Jeragh, B. & El-Asmy, A. A. Structure and spectroscopic studies of homo-and heterometallic complexes of adipic acid dihydrazide. *Spectrochim. Acta Mol. Biomol. Spectrosc.* **125**, 25–35 (2014).
54. Feng, J. et al. $CuFe_2O_4$ magnetic nanoparticles: A simple and efficient catalyst for the reduction of nitrophenol. *Chem. Eng. J.* **221**, 16–24 (2013).
55. Ismail, E., Sabry, D., Mahdy, H. & Khalil, M. Synthesis and characterization of some Ternary Metal Complexes of Curcumin with 1, 10-phenanthroline and their anticancer applications. *J. Sci. Res.* **6** (2014).
56. Kombaiah, K., Vijaya, J. J., Kennedy, L. J., Bououdina, M. & Al-Najar, B. Conventional and microwave combustion synthesis of optomagnetic $CuFe_2O_4$ nanoparticles for hyperthermia studies. *J. Phys. Chem. Solids* **115**, 162–171 (2018).
57. Zhao, L., Liu, H., Wang, F. & Zeng, L. Design of yolk–shell Fe_3O_4@ PMAA composite microspheres for adsorption of metal ions and pH-controlled drug delivery. *J. Mater. Chem. A* **2**, 7065–7074 (2014).
58. Fotukian, S. M., Barati, A., Soleymani, M. & Alizadeh, A. M. Solvothermal synthesis of $CuFe_2O_4$ and Fe_3O_4 nanoparticles with high heating efficiency for magnetic hyperthermia application. *J. Alloys Compd.* **816**, 152548 (2020).
59. Gupta, A. K., Mohanty, S. & Nayak, S. K. Preparation and characterization of lignin nanofibre by electrospinnig technique. *Int. J. Sci. Eng. Appl. Sci.* **1**, 184–190 (2015).
60. Safartoobi, A., Mazloom, J. & Ghodsi, F. Electrochemical and optical properties of magnetic $CuFe_2O_4$ nanofibers grown by PVP and PVA-assisted sol–gel electrospinning. *Appl. Phys. A* **128**, 13 (2022).
61. Rani, B. J. et al. Structural, optical and magnetic properties of $CuFe_2O_4$ nanoparticles. *J. Mater. Sci. Mater. Electron.* **29**, 1975–1984 (2018).

Acknowledgements

This work was supported in parts by the Kermanshah University of Medical Sciences Research Council (Grant No. 990592), Iran National Science Foundation (INSF) under Project No. 4028330, and Basic Science Research Program through the National Research Foundation of Korea (NRF) grant funded by the Ministry of Education (2021R1A6A1A03039211).

Author contributions

A.R. and N.F. proposed the main idea; N.F., F.A., A.H., S.M.H. carried out the experiments, characterization and write the article draft. A.R., A.R. and W.-K.J. charecterized the materials and revised the MS.

Declarations

Competing interests

The authors declare no competing interests.

Additional information

Correspondence and requests for materials should be addressed to A.R., A.R. or W.-K.J.

Reprints and permissions information is available at www.nature.com/reprints.

Publisher's note Springer Nature remains neutral with regard to jurisdictional claims in published maps and institutional affiliations.